On dislocation hardening in a new manufacturing route of fer-ritic ODS Fe-14Cr cladding tube

Freddy Salliot, Andras Borbely, Denis Sornin, Roland Logé, Gabriel Spartacus, Hadrien Leguy, Thierry Baudin, Yann Decarlan

materials

MDPI

Article

On dislocation hardening in a new manufacturing route of ferritic ODS Fe-14Cr cladding tube.

Freddy SALLIOT [1,*], András BORBÉLY [2], Denis SORNIN [1], Roland LOGÉ [3], Gabriel SPARTACUS [4], Hadrien LEGUY [1], Thierry BAUDIN [5] and Yann de CARLAN [1]

[1] Université Paris-Saclay, CEA, Service de Recherche en Matériaux et procédés Avancés, 91191, Gif-sur-Yvette, France
[2] Mines Saint-Etienne, Univ. Lyon, CNRS, UMR 5307 LGF, Centre SMS, F - 42023 Saint-Etienne, France
[3] Thermomechanical Metallurgy Laboratory (LMTM) –PX Group Chair, École Polytechnique Fédérale de Lausanne (EPFL), CH-2002 Neuchâtel, Switzerland
[4] Department of Materials Science and Engineering, KTH Royal Institute of Technology, SE-100 44 Stockholm, Sweden
[5] Université Paris-Saclay, CNRS, Institut de chimie moléculaire et des matériaux d'Orsay, 91405, Orsay, France
* Correspondence: salliot.freddy@gmail.com

Abstract: The microstructure evolution associated to the manufacturing of a Fe-14Cr-1W-0.3Ti-0.3Y_2O_3 grade ferritic stainless steel strengthened by dispersion of nano oxides (ODS) was investigated. The material was initially hot extruded, then shaped into cladding tube geometry via cold pilgering and stress release heat treatments. Each step of the process was analyzed to better understand the high microstructure stability of the material. Slight grain refinement and alpha <110> fiber texture reinforcement was obtained after cold pilgering. Despite high levels of stored energy the following heat treatment did not recrystallize the material. Only the Vickers hardness showed significant variations in the manufacturing steps, which was attributed to the recovery of statistically stored dislocations (SSD), as concluded from a combination of EBSD and X-ray diffraction measurements.

Keywords: ODS steel; Microstructure; Cold rolling; Dislocation density; X-ray diffraction; EBSD

1. Introduction

The development of the 4th generation of nuclear reactors is in progress world-wide. This generation meets the requirements of closing the lifecycle of nuclear fuels [1] while improving efficiency and safety. Thanks to substantial feedback since 1951 with the first reactor EBR-1 (Idaho), sodium cooled fast reactor (SFR) is the most advanced design. In this architecture, the reactor core environment is more severe than in pressurized water reactor. Parts inside the core are subjected to neutron flux causing more than 200 dpa and to operate at temperatures up to 650 °C [2,3].

Oxide dispersion strengthened (ODS) steels were identified since the 60s as promising candidates for SFR cladding tubes [4], and also for the first wall in fusion reactors. Indeed, the body-centered cubic matrix provides favorable resistance for creep and swelling under irradiation, and the homogenous dispersion of nano-oxides increases the mechanical properties at high temperature. The high chromium content in ferritic steels (>12 wt%) confers a better corrosion resistance compared to martensitic ones, but lowers the manufacturability.

Ferritic steel claddings are commonly shaped by cold working like pilgering to benefit from better geometrical accuracy [5–11]. Forming them is challenging since hardness higher than 400 HV1 may cause cladding cracks [7,12]. The absence of phase transformation in ferritic steel grades manufacturing requires high temperature

Citation: To be added by editorial staff during production.

Academic Editor: Firstname Lastname

Received: date
Revised: date
Accepted: date
Published: date

intermediate heat treatments in order to soften and recover the material between the pilgering steps. Because of cold pilgering, grains are elongated along the rolling direction (RD) and the <110> lattice directions become aligned with the RD (α fiber) [13]. These microstructural and textural anisotropies influence mechanical properties, inducing a higher strength [14–16].

Microstructures of ODS grades are very sensitive to the chemical composition. Ukai et al. [14] concluded that a content of Y_2O_3 lower than 0.25 wt.% leads to a recrystallized microstructure. This result has been confirmed by other studies [5,17] on Fe–12Cr–1.5W–0.26Ti–0.22Y_2O_3 cold rolled tubes. However, the grade Fe–15Cr–2W–0.3 Y_2O_3 that presents a higher Y_2O_3 content also exhibits a recrystallized microstructure [18].

This study highlights the microstructural stability of a Fe-14Cr (Fe-14Cr-1W-0.3Ti-0.3 Y_2O_3) ODS cladding tube during manufacturing. The investigated material is similar to 14YWT, which after extrusion at 850 °C, exhibits the ability to recrystallize as described in the standard CEA (The French Atomic Energy and Alternative Energy Commission) protocol in [8].

The newly proposed process route has been designed with 2 variations compared with the standard one: (i) a higher cumulated cross section reduction ratio than in [7] by using 2 successive passes and (ii) a removed stress release treatment compared to [7,8]. None of these changes, which allow a higher stored energy, led to the recrystallization of the material.

Several microstructural indicators were analyzed, such as nano-oxides volume fraction, grain size, crystallographic texture and geometrically necessary dislocation (GND) densities from EBSD to understand hardness variation through steps. In addition, X-ray line profile analysis (LPA) has been used to investigate the impact of stress release treatment on dislocation density.

2. Materials and Methods

2.1. Materials and shaping

This paper focuses on a Fe-14Cr-1W-0.3Ti-0.3Y_2O_3 grade steel obtained by powder metallurgy. In this process, a pre-alloyed ferritic matrix powder (Fe, Cr, W, Mn, Ni …) is ball milled with powders of Y_2O_3 and TiH_2. Then, the powders are consolidated by hot extrusion. For this grade, powders and mother tube are manufactured with the same parameters as in a previous study of Toualbi et al. [7]. The processing route has been designed with moderate straining by cold rolling passes (with a cumulated logarithmic reduction ratio of ~40%) and intermediate heat treatment of 60 min at 1200 °C (Figure 1).

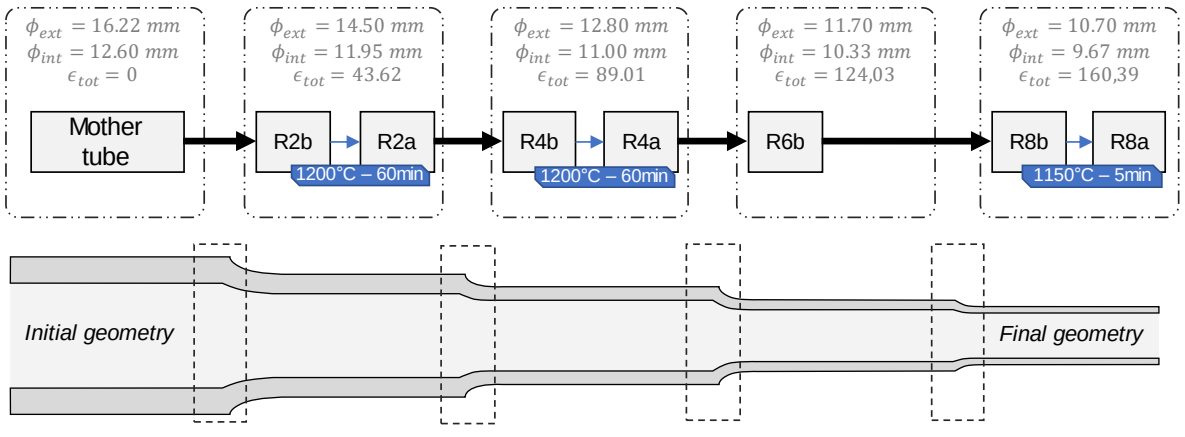

Figure 1. Denomination of the tube states during the rolling process.

The samples are named according to the rolling pass number followed by "b" or "a" respectively for "before" and "after" heat treatment under He atmosphere. Ultimately, the mother tube is cold pilgered via high precision tube rolling (HPTR) down to 500 µm wall thickness. The chemical composition is given in **Table 1**.

Table 1. Chemical composition of Fe-14Cr studied grade.

	Content (wt.%)										
Fe	C	Cr	Mn	Mo	Ni	Si	Ti	W	Y	N	O
Bal.	0.013	14	0.25	0.005	0.33	0.28	0.27	1.1	0.15	0.015	0.13
	±0.001	*±0.6*	*±0.02*	*±0.001*	*±0.05*	*±0.01*	*±0.01*	*±0.27*	*±0.04*	*±0.0005*	*±0.01*

2.2. Experimental techniques

All analyzed samples were taken from one cladding tube, extracted after each step of the shaping process.

Vickers hardness tests were performed on an Innovatest Falcon 500 durometer with 1 kgf load on the longitudinal [RD, normal direction (ND)] plane (Figure 2). Samples were polished until mirror surface finishing (with 1 µm diamond paste) prior to hardness testing.

Microstructural and texture characterizations were made via EBSD. Data were acquired with a SEM-FEG Zeiss SIGMA HD equipped with an Oxford fast EBSD detector, and were analyzed with the EDAX-OIM software. The final preparation of EBSD samples was an electrochemical polishing that removes the hardened layer induced by diamond polishing. Orientation maps were acquired on the transverse [ND, transverse direction (TD)] plane to analyze more grains near the external skin (Figure 2). Orientation maps were acquired with 20 kV acceleration voltage and a 35 nm step size on 21x28 µm² area size. Texture calculations were performed using the generalized spherical harmonic series expansion approach. Calculations were performed with 34 coefficients and a 5° Gaussian half width.

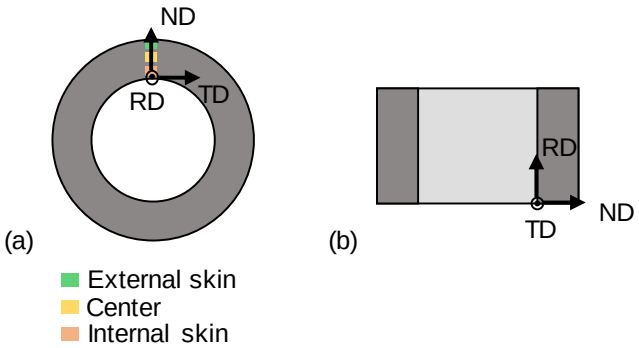

Figure 2. (a) Transverse section with the zones of interest; (b) longitudinal section.

Small angle X-ray scattering (SAXS) experiments were performed on ODS steels to characterize the nano-sized oxide dispersion in the ferritic matrix. Following the same parameters as a similar study [19], data were acquired on a laboratory setup at CEA. A Mo anode X-ray source was used (wavelength of 0.07107 nm) with a beam size of ~ 1 mm². Samples were polished down to 80 µm thickness according to the beam energy to obtain sufficient transmission signal (10 - 20 % of the incident intensity).

Each SAXS measurement consists of a two-dimensional pattern, which was azimuthally integrated, background subtracted and normalized by the incident flux,

specimen thickness, transmission and solid angle viewed by the detector. Intensity was reduced to absolute units using a glassy carbon secondary standard (NIST - SRM 3600). To extract the mean radius and volume fraction, the SAXS data were fitted by a model described in [20] taking into account a lognormal distribution of spheres with a dispersion of 20 % [21]. More calculation details are available in [22–24].

X-Ray diffraction (XRD) patterns were acquired at the beam line P21.2 of the Petra III – DESY synchrotron (Hamburg). The X-ray energy was 83 keV and a beam size of 150 x 150 μm² was used. A Linkam TS1500V oven heated sample up to 1200 °C at a rate of 200 °C/min. For evaluation, the 2D XRD patterns were azimuthally integrated. The instrumental broadening was measured with a NIST LaB6 standard (SRM 660a). The modified Warren-Averbach method (mWA) was used to estimate dislocation density as described in [25]. The mWA method links the amplitude of the Fourier coefficients $A(n)$ of the line profile to the dislocation density ρ following equation (1).

$$\ln\big(A(n)\big) \cong A^S(n) - \rho B n^2 \ln\left(\frac{R_e}{n}\right)(K^2C) + QB^2n^4 \ln\left(\frac{R_1}{n}\right)\ln\left(\frac{R_2}{n}\right)(K^2C)^2 \qquad (1)$$

Where $A^S(n)$ is the small crystallite size contribution to broadening [25], n is the Fourier parameter and $B = \pi b^2/2$ with b the magnitude of the Burgers vector. R_e is the outer cut-off radius (or screening length) of the dislocation ensemble, while R_1 and R_2 are parameters with length dimension, but no physical interpretation.
$K = 2\sin(\theta)/\lambda$, with λ the X-ray beam wavelength and θ the Bragg angle. The dislocation contrast factor C of each diffraction peak was calculated with ANIZC [26] using theoretical elastic constants for a ferromagnetic Fe-Cr alloy at 15 at.% Cr [27] and the assumption that edge and screw dislocations are present in equal proportion. The factor $Q = (\overline{\rho^2} - \bar{\rho}^2)/2$ represents the fluctuation of the dislocation density.
It was shown recently that the full width at half maximum (FWHM) of the peaks is strongly influenced by the arrangement of dislocations [28] and this broadening better approximates the stored energy than the value which considers R_e evaluated from eq. (1) [29]. Its physical reason relies on the fact that eq. (1) is the asymptotic approximation of the Fourier transform of the peak profile valid at small n, which is in contradiction with the long range interaction length between dislocations that determines their screening distance. For example, for a system of randomly arranged edge dislocation dipoles the value of R_e obtained from eq. (1) overestimates the true screening length by one order of magnitude [27]. Therefore, the strain energy and the corresponding screening length R_e was evaluated using the modified Williamson-Hall method (mWH):

$$\Delta K = \left(\frac{A_D}{D}\right) + \left[\frac{b^2}{4\pi}\rho \ln\left(\frac{R_e}{r_0}\right)\right]^{1/2} K\sqrt{C} + O(K\sqrt{C})^2 \qquad (2)$$

Where $K = 2\sin(\theta)/\lambda$, $\Delta K = FWHM\cos(\theta)/\lambda$ and the inner cut-off radius r_0 was taken equal to $2.6\,b$ [30].

3. Results and discussion

3.1. Hardness evolution during the manufacturing route

The processing route was designed at CEA to reduce the mother tube (MT) to the final section by cold rolling, without damaging the tube by crack formation. The various intermediate steps are referenced in Figure 1. Total strain ε_{tot} is defined as the logarithmic ratio of the surfaces before and after rolling. Associated hardness values are drawn in Figure 3. Obviously, each pilgering step implies hardening, while each heat treatment softens the material.

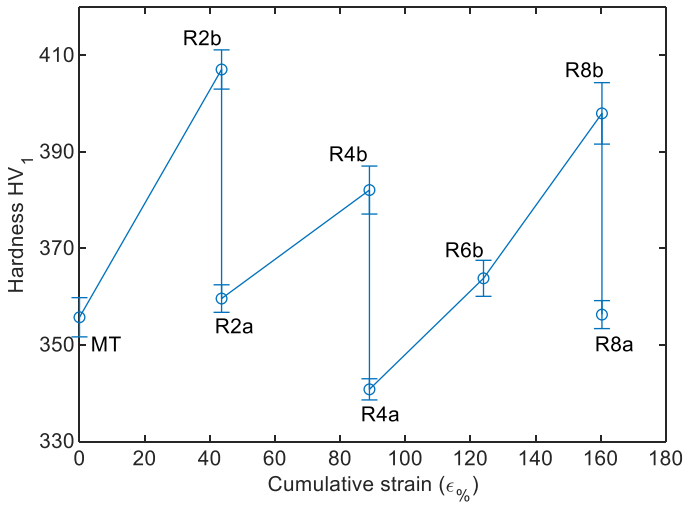

Figure 3. Vickers hardness at each step of the process.

3.2. Microstructural evolution

3.2.1. Nano-oxides

SAXS has been used to measure nano-oxide size and volume fraction evolutions. Samples with α fiber texture were analyzed with the RD aligned with the X-ray beam direction to avoid elliptic SAXS pattern related to the material texture. Assumption was made on $Y_2Ti_2O_7$ pyrochlore as the only nano-oxides phase for the estimation of the volume fraction (f_V), as it is the most commonly identified phase in the literature [31–33]. R8* is a sample similar to R8a with a 750 °C for 30 min long heat treatment. Results are displayed in **Table 2** and show a slight increase of the nano-oxides mean radius (R_m) during the manufacturing from 1.4 nm to 2.0 nm. Taking into account the thermal history of consolidation and extrusion of the material to obtain MT state, the initial radius obtained is in agreement with radius observed or calculated in [20,34,35] after heating up to 1100 °C.

Table 2. Volume fraction and mean radius of Y2Ti2O7 nano-oxides calculated from SAXS signal. Standard deviation is linked to the calculated dispersion.

	MT	**R2a**	***R8****
Volume fraction (%)	0.36 ± 0.09	0.33 ± 0.08	0.26 ± 0.07
Mean radius (nm)	1.4 ± 0.2	1.8 ± 0.2	2.0 ± 0.1

The growth of the nano-oxides is most likely due to coalescence during the successive thermal treatments as the volume fraction seems to remain constant. Mean radius variations remain small as $Y_2Ti_2O_7$ pyrochlore is known to exhibit a strong stability against coarsening even at high temperature [36,37]. Knowing that nano-oxide density N can be calculated with equation (3) it comes to $N \approx 10^{23}$-10^{24} m^{-2} in agreement with previous TEM observations [32].

$$N = \frac{f_V}{\frac{4}{3}\pi R_m^3} \quad (3)$$

This high-density exerts high Zener pressure at every step of the manufacturing, and is responsible for grain boundary and dislocation pinning [38,39].

3.2.2. Grain size, texture and dislocation density

EBSD is a powerful method to extract microstructure and texture data from orientation maps. Analyses were performed on each step of the forming process on the [ND, TD] section to characterize their evolutions. Grain boundary was defined by considering a disorientation greater than 10°. Grain size is mostly below 5 µm equivalent diameter (D) with a non-Gaussian distribution. So, three grain populations are studied to compare microstructures: D < 0.5 µm, D > 1 µm and the population between. Figure 4 depicts these three population variations through shaping route. Mean equivalent diameter is also given as a comparative tool. Bigger grains (D > 1 µm) decrease in number but also in area fraction, meaning bigger grains are subdivided during the whole process. Thus, smaller grains (D < 0.5 µm) double in number and their area fraction after increases after each cold rolling pass, impacting the mean grain size of the cladding. Microstructure tends to be more fine-grained when adding deformation cycles (Figure 5).

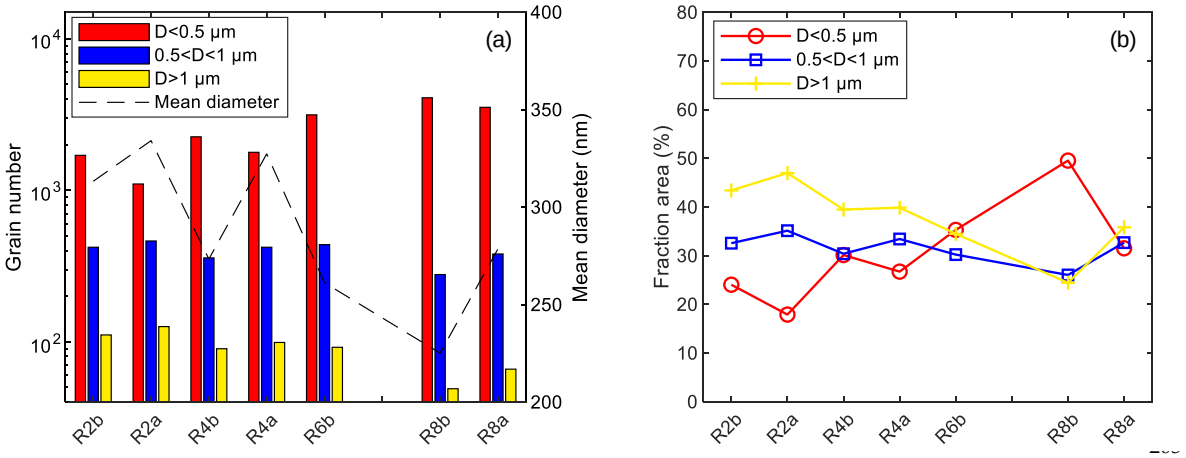

Figure 4. Evolution of mean diameter and grain populations in [ND, TD] section, near external skin through shaping process (a) in number; and (b) in area fraction.

Body centered cubic (BCC) materials are well known to develop α fiber texture during rolling. The corresponding grains have the crystallographic directions <110> aligned with RD [38]. This fiber is induced by extrusion [40] and is reinforced by pilgering. Regarding the outer skin, the fiber remains complete throughout the process (Figure 5) with a {111}<110> reinforcement. However, the preferential orientation tends to shift towards the {112}<110> orientation through steps. These small and elongated (in RD) morphologies are not the most favorable for creep strength [41], but even heat treatments at 1250 °C, at whatever moment in the fabrication route, do not recrystallize the microstructure.

Texture evolution is consistent with previous work, which evidenced the formation of a strong incomplete fiber (between {001}<110> and {111}<110>) during cold rolling of different BCC materials. Raabe and Lücke [40] report in the case of low-carbon steels, a dominance of the fiber components {001}<110> and {112}<110>.

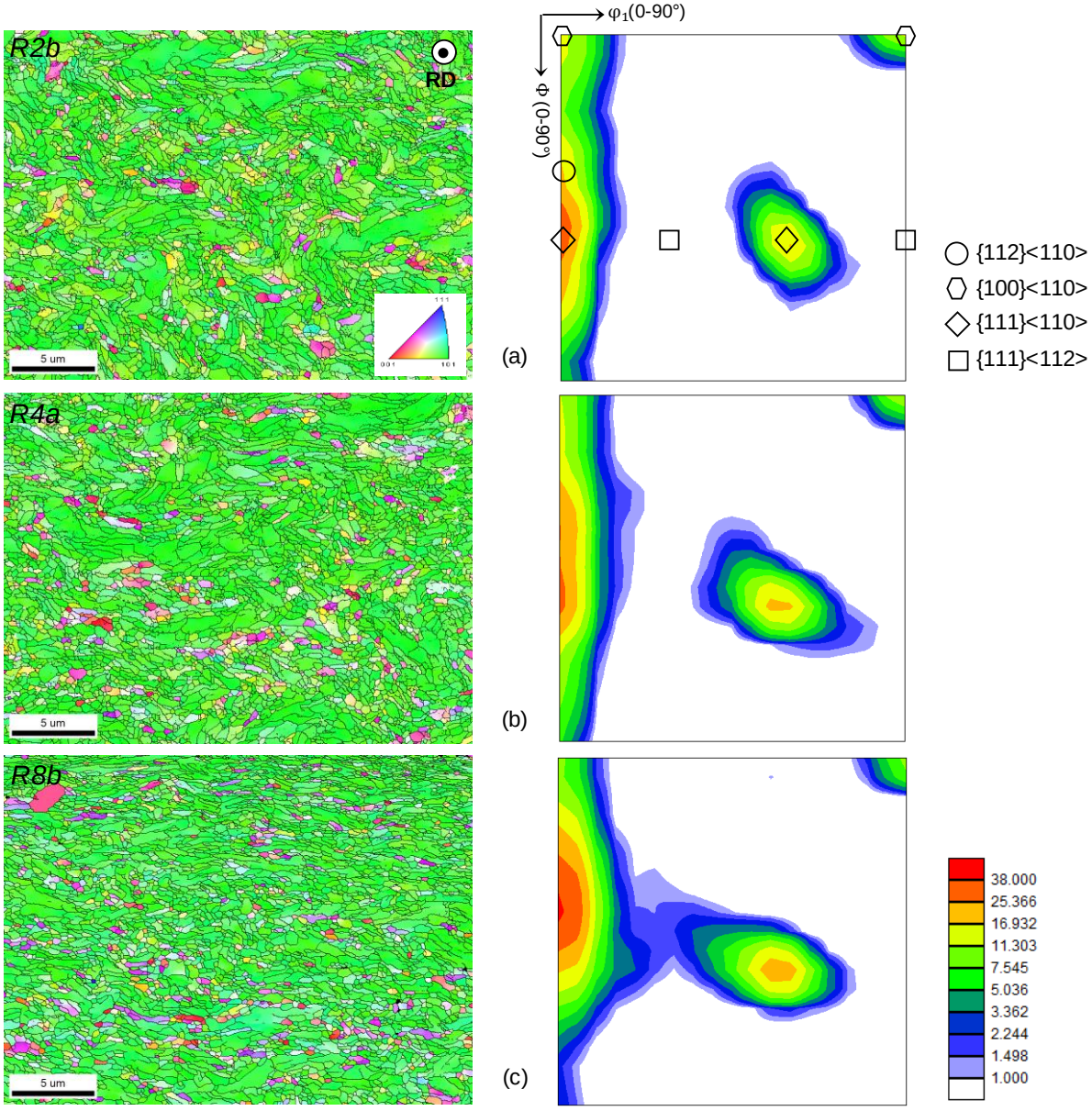

Figure 5. RD-IPF on left side and Euler section at φ_2=45° at external skin on right side for (a) R2b; (b) R4a and (c) R8b steps.

EBSD can also be used to calculate the geometrically necessary dislocation (GND) density [44]. Ashby [45] differentiates GNDs as dislocations tilting the crystal lattice to accommodate plastic strain and statistically stored dislocations (SSDs), which are randomly trapped dislocations that do not affect the orientation of the crystal lattice. So, only GND can be detected by conventional EBSD and the lattice curvature is used to obtain their density ρ_{GND}. In this study the Nye's tensor has been evaluated with the first neighbor, according to the method described in [46].

The evolution of average ρ_{GND} over the manufacturing process was evaluated at the center, at the internal skin and at the external skin of the tube and is presented in Figure 6. The error bars correspond to the standard deviation. ρ_{GND} stays mostly constant and high (~ $1 \cdot 10^{15}$ m^{-2}). No clear fluctuation was found between the three sites, but low variation can be considered between deformation and heating steps, even if those variations remain significantly lower than the error bars.

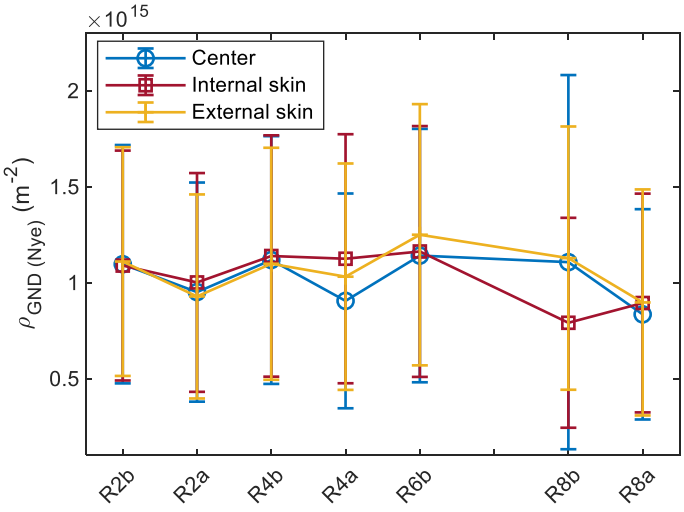

Figure 6. Average GND densities during the shaping process calculated by Nye's tensor method for different sites.

3.2.3. Hardening contributions

Studied microstructural parameters are well known to contribute to the yield strength, and their contributions are usually added $\sigma_{YS} = \sigma_0 + \sigma_{SS} + \sigma_{GB} + \sqrt{\sigma_P^2 + \sigma_D{}^2}$ with σ_0 the Peierls-Nabarro's stress, σ_{SS} the solid solution contribution, σ_{GB} the contribution of grain boundaries, σ_P that of nanoparticles and σ_D the dislocation hardening [47,48]. According to Tabor [49] "the Vickers hardness is equal to the flow stress of a test specimen after it has been plastically strained an additional 8 %". Also, σ_{YS} has been experimentally found to be proportional to the hardness [50], with σ_{YS}(MPa) = Hardness(MPa)/3 (1 HV_1 = 9.81 MPa).

σ_0 was calculated according to the Peierls-Nabarro equation:

$$\sigma_0 = M\frac{2\mu}{1-\nu}\exp\left(\frac{-2\pi a}{b(1-\nu)}\right) \quad (4)$$

Where M is the mean Taylor factor (M = 2.5 for textured material), μ and ν are the shear modulus (81 GPa) and the Poisson's ratio (0.3) respectively. a and b are respectively the lattice parameter and the modulus of the Burgers vector. σ_0 = 18 MPa in this study.

σ_{SS} was estimated based on the Lacy and Gensamer relation [51] $\sigma_{SS} = \sum_i k_i X_i^Z$. k_i and X_i are respectively the atomic concentration and the hardening constant associated with each atom i. The exponent Z depends on the nature of the element in solution. It is 0.5 for insertion elements and 0.75 for larger elements in substitution. σ_{SS} was 145 MPa according to chemical composition (Table 1).

The nano-oxides contribution σ_P was estimated with the modified Orowan equation proposed by Martin [52]:

$$\sigma_P = \frac{0.81M\mu b}{2\pi(1-\nu)^2}\ln\left(\frac{1}{b}\sqrt{\frac{2}{3}}R_m\right)\Big/\sqrt{\frac{2\pi}{3f_V}R_m} \quad (5)$$

Using R_m and f_V values from Table 2 gives $\sigma_P(MT)$= 350 ± 61 MPa, $\sigma_P(R2a)$= 304 ± 52 MPa and $\sigma_P(R8^*)$= 257 ± 42 MPa.

Regarding the previous microstructural indicators, only (i) grain boundary strengthening and (ii) work hardening are considered in micro-hardness variations since the solid solution hardening and σ_0 are not expected to change. Moreover, σ_P evolution cannot lead to changes in the measured hardness.

(i) Concerning the grain boundaries, the Hall-Petch effect is well known to explain the dependency of the yield stress (or hardness) with grain size [53]. To overcome the non-gaussian distribution of grain size, the Hall-Petch model modified by Srinivasarao et al. [54] was used.

$$\sigma_{GB} = 0.2\mu\sqrt{b}\sum_i f_i^{area}/\sqrt{D_i} \quad (6)$$

where f_i^{area} is the area fraction of grains with a diameter D_i. EBSD data were used to calculate σ_{GB}.Values are displayed in Figure 7. The grain boundary contribution to yield strength evolves similary to hardness variations through all thermomechanical steps. σ_{GB} increases during pilgering steps (from MT to R2b) and decreases during annealing (from R8b to R8a). However, MT and R8a show similar hardness values (Figure 3) with a higher difference between $\sigma_{GB}(MT)$ and $\sigma_{GB}(R8a)$ than between successive steps $\sigma_{GB}(MT)$ and $\sigma_{GB}(R2a)$. Hardness evolution cannot be fully explained by the Hall-Petch law.

(ii) In pure face centered cubic (FCC) crystals, the hardness is proportional to $\sqrt{\rho}$ throught the Taylor's relation $\sigma_D = 0.3M\mu b\sqrt{\rho}$. For BCC phases like Fe-14Cr, this relation is not as clear as for FCC [55]. The GND density assessed by EBSD does not vary significantly (Figure 6), and considering their participation alone leads to estimation close to $\sigma_{D_{GND}}$ = 470 MPa (Figure 7). Many theoretical or experimental studies have been performed on FCC materials to correlate the amount of GND and SSD densities and their respective participation in work hardening, but no consensus has been found [45,55–58].

Finally, the GND density seems to saturate, however, it shows a very slight increase through pilgering steps, and a decreases upon heat treatment (Figure 6).

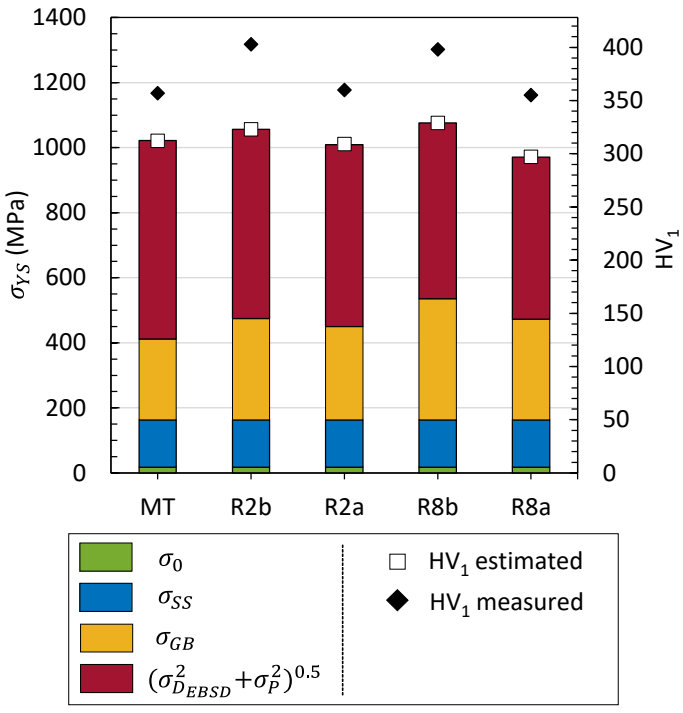

Figure 7. Estimated yield strength and hardness from microstructural contributions. Precipitate contribution $\sigma_P(R2b)$ is taken equal to $\sigma_P(MT)$ by assumption on a limited nano-oxides distribution evolution through cold pilgering step. The same for $\sigma_P(R8b)$ taken equal to $\sigma_P(R8a)$.

By considering all these microstructural contributions, the estimated hardness values are underestimated and do not fluctuate as much as the measured ones (Figure 7). This is particularly true for variations through heat treatment (from R2b to R2a, and from R8b to R8a). At this point, none of the microstructural contributions showed any significant variation which could explain this evolution.

3.2.4. Heat treatment behavior

In order to characterize the microstructure stability at various temperatures, a thorough study has been performed on the sample corresponding to the last processing step R8b. In addition, samples were maintained at the desired temperature for different durations under helium atmosphere, followed by helium quench. As no significant evolution was noticed on grain size distribution, hardness was used to analyze impact of heat treatment (Figure 8).

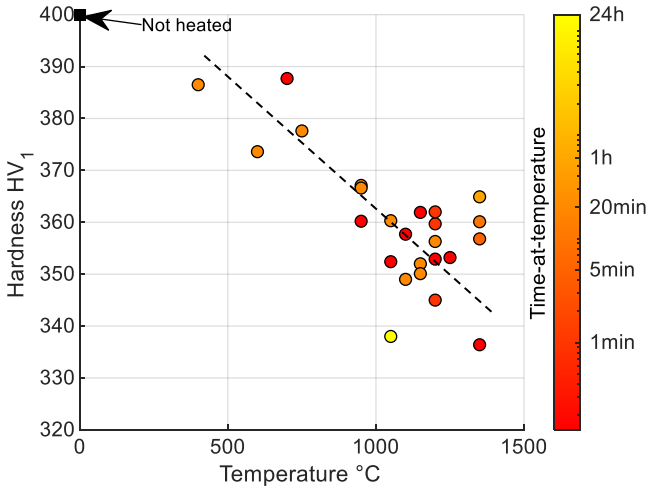

Figure 8. Hardness of R8b heated with various parameters.

First, little softening is noticed until 400 °C. Then, for higher temperatures, hardness can be considered as linearly decreasing with temperature. Finally, only the temperature seems to affect hardness at first order, without any variation of microstructure observed by EBSD. Based on this result, heat treatments lasting less than few hours can be wisely chosen in the manufacturing route to soften the cladding before pilgering (Figure 8). Moreover, since extreme treatments (fast kinetics and low holding time) impact hardness as much as moderate ones, dislocation recovery is more likely to be responsible for hardness decrease than slower mechanisms such as chemical diffusion. Since the GND density remains stable even after 5 min at 1150 °C (Figure 6), the SSD contribution must be considered.

The R8b sample was analyzed by XRD at beamline of Petra III - DESY, in order to estimate SSD density during heating. Considering the most severe treatment possible, the sample was heated at a rate of 200 °C/min, up to 1200 °C. Acquisition of diffraction patterns was done every second. In-situ obtained average diffractograms (integrated over the azimuthal angle of the 2D detector) at 55 °C and 1200 °C are shown in Figure 9. The decrease of the intensity at higher 2θ during heating is caused by the Debye-Waller effect. Due to its low intensity, the 222 peak was not taken into account in the analysis. The 110 peak contains more than 75 % of counted photons due to the strong α fiber texture.

The dislocation density from the mWA analysis drops from $3.8\ 10^{15} \pm 1.2\ 10^{14}$ m^{-2} to $5.1\ 10^{14} \pm 1.8\ 10^{14}$ m^{-2} during heating (Figure 10-a). Since density near 10^{13} m^{-2} is expected in recrystallized materials, it is concluded that only recovery occurs in the sample.

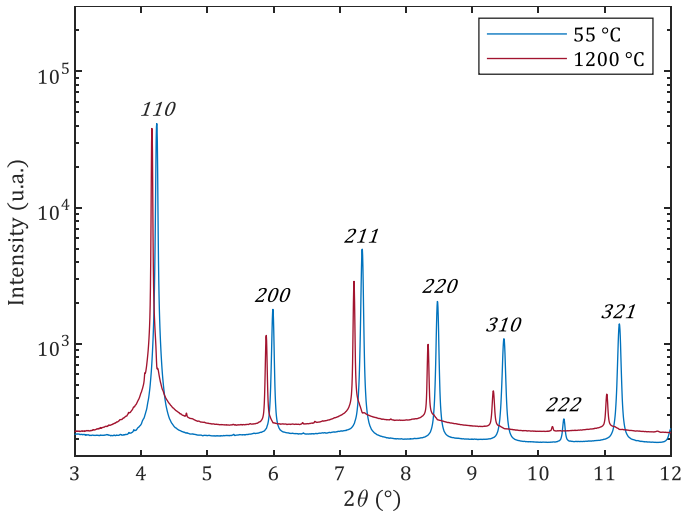

Figure 9. Average synchrotron X-ray diffractograms spectra measured on R8b at 55°C and 1200°C.

The stored energy (SE) takes into account dislocation density but also dislocation arrangement and can be directly obtained from mWH-plot [29]. Based on Figure 10-a and Figure 10-b, the SE shows a similar behavior to the dislocation density. It remains stable from room temperature to about 300 – 400 °C, then both drop until 650 °C. Combining the SE values with the dislocation density given by the mWA method, the screening parameter R_e and the interaction parameter $M_W = R_e\sqrt{\rho}$ [59] can be calculated (Figure 10-d and Figure 10-c, respectively).

- From the room temperature to 400 °C, ρ_{XRD} decreases and M_W increases (Figure 10-c). The latter describes the average dislocation [29]. The increase in it both Re and M_W can be understood in terms of the annihilation of dislocation dipoles for which Re is small [29]. Although both the dipoles and subgrain boundaries have a small M_W, the latter are stable structures at high temperatures as seen before with ρ_{GND} evolution.

- From 400 to 600 °C, both ρ_{XRD} and M_W decline slightly. This means that SSD start to annihilate with a faster kinetics than bellow 400 °C. Since M_W and R_e are decreasing (Figure 10-d), assumption can be made on the disappearance of dislocations with longer screening length. In addition, some dislocations can rearrange into GND structures (with lower energy), also leading to the decrease of M_W and R_e.

- The 650 – 700 °C temperature range corresponds to the sample Curie point measured by calorimetry for this sample. Anomalous behavior in the lattice parameters [60] and also in diffusion kinetics are well known around the Curie point in ferritic stainless steels. In the studied alloy these changes are local and since the material did not transform completely to FCC phase (small austenite peak is visible near the 110 refection above 800 °C, Figure 9) they could induce extra strain affecting peak broadening. As the measurements were acquired during heating, crossing the Curie point this anomalous behavior could lead to the observed increase in M_W and R_e describing the dislocation rearrangement. The interpretation of these parameters above 600 °C is not possible. This austenitic phase disappears again after cooling.

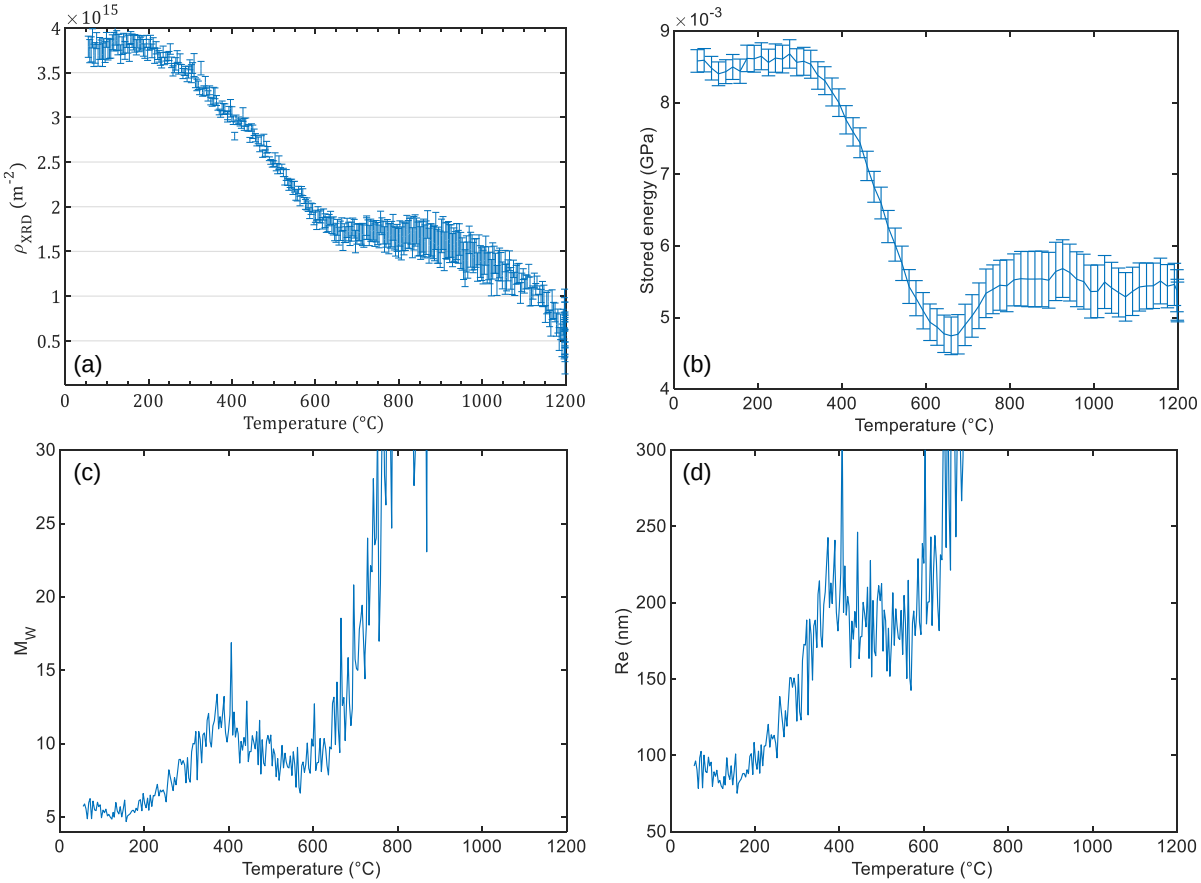

Figure 10. Evolution of (a) dislocation density, (b) stored energy, (c) the $M_W = R_e\sqrt{\rho_{XRD}}$ parameter, and (d) R_e during the heating from mWA and mWH calculations

Table 3 lists the dislocation density estimated from EBSD and mWA of the sample before heat treatment (R8b), and after heat treatment (R8a). Both XRD acquisitions were performed at 55 °C, others at room temperature. The GND density measured by EBSD was slightly reduced, while ρ_{XRD} was divided by about 8. This reduction can be attributed to SSD density.

Table 3. Dislocation density before and after heating up to 1200 °C at +200 °C/min obtained from EBSD and XRD (calculated with the mWA method).

	R8b	**R8a**
$\boldsymbol{\rho_{EBSD}}$ **(10^{15} m^{-2})**	1.0±0.6	0.8±0.5
$\boldsymbol{\rho_{XRD}}$ **(10^{15} m^{-2})**	3.8±0.2	0.5±0.2

Assuming that the nano-oxide distribution does not evolve during this relatively rapid heat treatment, the $\left(\sigma_{D_{total}}^2 + \sigma_P^2\right)^{0.5}$ contribution was estimated, as well as the yield strength and Vickers hardness (Figure 11).

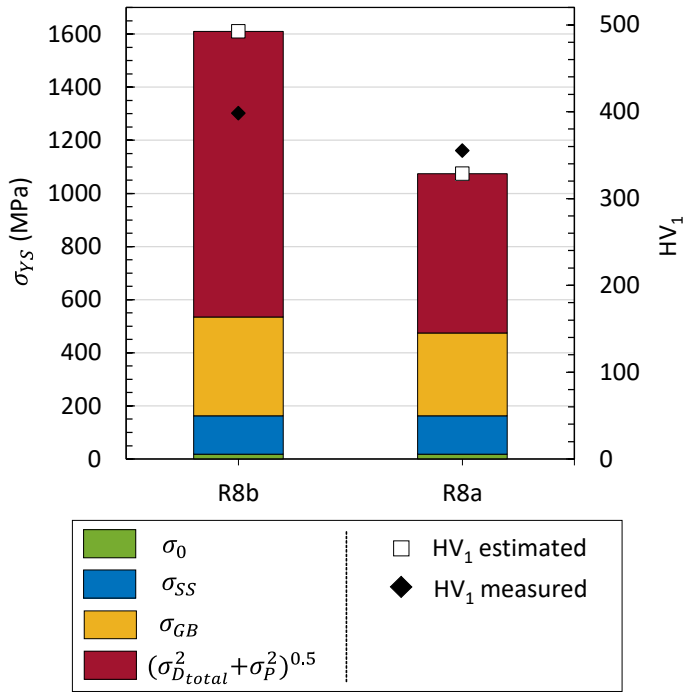

Figure 11. Estimated yield strength and hardness from complete microstructural contributions before and after heating up to 1200 °C at +200 °C/min. Precipitate contribution is taken constant.

- Hardening models

Taking ρ_{XRD} into account results obviously in a greater variation in estimated yield strength and therefore in the estimated hardness, than with only GND. In the case of R8a (Figures 7 and 11), the estimated hardness goes from 297 HV$_1$ (EBSD) to 329 HV$_1$ (EBSD + XRD) for an experimental value of 355 HV$_1$. Thus, softening during annealing seems to be mainly controlled by SSDs in this highly strained and textured BCC material since the GND density does not evolve significantly.

Also, for R8b the estimated hardness rises from 329 HV$_1$ (EBSD) to 492 HV$_1$ (EBSD + XRD) for an experimental value of 398 HV$_1$. Then, yield strength (and hardness) is overestimated. This can be due to several approximations.

The Taylor's relation $\sigma_D = \alpha M \mu b \sqrt{\rho}$ seems not to be the right description for these materials since differences between measured and estimated hardness values are still large. The average value of the Taylor factor M could be reconsidered (i) even though it has little impact on the estimates, as could the α-factor (ii) (here fixed at 0.3) which can vary if the dislocation structure changes [61,62]. Also, (iii) the total dislocation density may be underestimated. According to [29] the asymptotic mWA allows a reliable evaluation of the dislocation density if the local distance between dislocations is larger than of about 30 nm, which corresponds to a total dislocation density of 10^{15} m^{-2}. This means that in the case of Fe-14Cr the XRD method cannot characterize dislocation density in subgrain and grain boundaries with disorientations larger than ~0.5°. For this reason, the mWA XRD method underestimates the total dislocation density. Finally, (iv) the Tabor's relation remains an empirical law whose coefficient depends on the material.

- Microstructural evolution

Taking into account the evolution of the presented microstructural indicators, only the variation of SSDs and GNDs with a disorientation < 0.5° seem to be responsible for the evolution of cladding hardness during the manufacturing process.

4. Conclusion

The Fe-14Cr-1W-0.3Ti-0.3Y_2O_3 grade developed at CEA exhibits high microstructure stability when being manufactured. The nano-oxide reinforcement obtained with the Y_2O_3 content, higher than 0.25 %, limits the grain recrystallization. Stability of the microstructure persists up to 1200 °C.

Only slight variations are noticed in all studied microstructure indicators such as grain size, nano-oxide coalescence, texture and GND density. Hardness evolves as expected, according to heat treatments and deformation stages, while remaining around 400 HV_1 such as to avoid cracking. Moreover, hardness decrease is mostly controlled by the heat treatment temperature, and not by its holding time.

By using synchrotron X-ray, peak narrowing has been quantified. SSD variation in such highly deformed BCC alloy is identified to have a major contribution in the measured hardness variations through thermomechanical steps.

5. Patents

Author contributions: Freddy SALLIOT: Writing - Original Draft, Investigation, Visualization, Methodology, Formal analysis, Software, Validation, András BORBÉLY: Writing - Review & Editing, Methodology, Formal Analysis, Denis SORNIN: Writing - Review & Editing, Ressources, Supervision ,Roland LOGÉ: Writing - Review & Editing, Supervision, Gabriel SPARTACUS: Writing - Review & Editing, Software, Hadrien LEGUY: Investigation, Thierry BAUDIN: Writing - Review & Editing, Supervision, Yann de CARLAN: Writing - Review & Editing, Supervision, Funding acquisition.

Funding: This research received no external funding.

Institutional Review Board Statement: Not applicable.

Informed Consent Statement: Not applicable.

Data Availability Statement: The data that support the findings of this study are available on request from the corresponding author FS.

Acknowledgments: Authors would like to thank Frederic Bondiguel and David Soumet for manufacturing our tube, Thomas Guilbert for his help in heat treatments and Elodie Rouesne for her support in sample preparation and EBSD guidance.

Authors also acknowledge Malte Blankenburg and the scientific team of P21 beamline of the DESY synchrotron, and Raphaëlle Guillou, Emilien Guy, Emma Kruck and Joël Malaplate for their participation on beam time.

This research is funded by the Reactors of 4th Generation (R4G) program of the French Alternative Energies and Atomic Energy Commission (CEA).

RL acknowledges the generous sponsoring of PX Group to the LMTM laboratory.

Conflicts of Interest: The authors declare no conflicts of interest.

References

1. DOENE (USDOE Office of Nuclear Energy, Science and Technology (NE)), Generation IV International Forum, A Technology Roadmap for Generation IV Nuclear Energy Systems, 2002. https://doi.org/10.2172/859029.
2. F. Carré, P. Yvon, P. Chaix, Innovative reactor systems and requirements for structural materials, in: Nuclear Energy Agency, Organisation for Economic Co-operation and Development, Karlsruhe, Germany, 2008: pp. 39–47.
3. P. Yvon, F. Carré, Structural materials challenges for advanced reactor systems, J. Nucl. Mater. 385 (2009) 217–222. https://doi.org/10.1016/j.jnucmat.2008.11.026.
4. J.-J. Huet, Possible fast reactor canning material strengthened ans stabilized by dispersion, Powder Metall. 10 (1967) 208–215. https://doi.org/10.1179/pom.1967.10.20.010.
5. T. Narita, S. Ukai, T. Kaito, S. Ohtsuka, T. Kobayashi, Development of Two-Step Softening Heat Treatment for Manufacturing 12Cr--ODS Ferritic Steel Tubes, J. Nucl. Sci. Technol. 41 (2004) 5.
6. A. De Bremaecker, Past research and fabrication conducted at SCK•CEN on ferritic ODS alloys used as cladding for FBR's fuel pins, J. Nucl. Mater. 428 (2012) 13–30. https://doi.org/10.1016/j.jnucmat.2011.11.060.

7. L. Toualbi, P. Olier, E. Rouesne, D. Bossu, Y. de Carlan, On the Influence of Cold Rolling Parameters for 14CrW-ODS Ferritic Steel Claddings, Key Eng. Mater. 554–557 (2013) 118–126. https://doi.org/10.4028/www.scientific.net/KEM.554-557.118.
8. C.P. Massey, P.D. Edmondson, M.N. Gussev, K. Mao, T. Gräning, T.J. Nizolek, S.A. Maloy, D. Sornin, Y. De Carlan, S.N. Dryepondt, D.T. Hoelzer, Insights from microstructure and mechanical property comparisons of three pilgered ferritic ODS tubes, Mater. Des. 213 (2022) 110333. https://doi.org/10.1016/j.matdes.2021.110333.
9. Y.C. Kim, H.J. Jin, S.H. Noh, S.H. Kang, B.K. Choi, K.B. Kim, G.E. Kim, T.K. Kim, Microhardness and microstructure of Ferritic-Martensitic ODS steel tube fabricated by a pilger process, in: Jeju, Korea, 2016.
10. S.M.S. Aghamiri, T. Sowa, S. Ukai, N. Oono, K. Sakamoto, S. Yamashita, Microstructure and texture evolution and ring-tensile properties of recrystallized FeCrAl ODS cladding tubes, Mater. Sci. Eng. A. 771 (2020) 138636. https://doi.org/10.1016/j.msea.2019.138636.
11. P.K. Parida, A. Dasgupta, S.K. Sinha, Comparison of Microstructure and Microtexture Evolution in 9Cr and 18Cr Oxide Dispersion-Strengthened Steels during Fuel Clad Tube Fabrication, J. Mater. Eng. Perform. 30 (2021) 9227–9236. https://doi.org/10.1007/s11665-021-06108-1.
12. M. Inoue, T. Kaito, S. Ohtsuka, Research and Development of Oxide Dispersion Strengthened Ferritic Steels for Sodium Cooled Fast Breeder Reactor Fuels, (2007). https://doi.org/10.1007/978-1-4020-8422-5_16.
13. A. Alamo, H. Regle, G. Pons, J.L. Béchade, Microstructure and Textures of ODS Ferritic Alloys Obtained by Mechanical Alloying, Mater. Sci. Forum. 88–90 (1992) 183–190. https://doi.org/10.4028/www.scientific.net/MSF.88-90.183.
14. S. Ukai, T. Nishida, H. Okada, T. Okuda, M. Fujiwara, K. Asabe, Development of Oxide Dispersion Strengthened Ferritic Steels for FBR Core Application, (I): Improvement of Mechanical Properties by Recrystallization Processing, J. Nucl. Sci. Technol. 34 (1997) 256–263. https://doi.org/10.1080/18811248.1997.9733658.
15. S. Ukai, T. Nishida, T. Okuda, T. Yoshitake, Development of Oxide Dispersion Strengthened Steels for FBR Core Application, (II): Morphology Improvement by Martensite Transformation, J. Nucl. Sci. Technol. 35 (1998) 294–300. https://doi.org/10.1080/18811248.1998.9733859.
16. B. Fournier, A. Steckmeyer, A.-L. Rouffie, J. Malaplate, J. Garnier, M. Ratti, P. Wident, L. Ziolek, I. Tournie, V. Rabeau, J.M. Gentzbittel, T. Kruml, I. Kubena, Mechanical behaviour of ferritic ODS steels – Temperature dependancy and anisotropy, J. Nucl. Mater. 430 (2012) 142–149. https://doi.org/10.1016/j.jnucmat.2012.05.048.
17. T. Narita, S. Ukai, B. Leng, S. Ohtsuka, T. Kaito, Characterization of recrystallization of 12Cr and 15Cr ODS ferritic steels, J. Nucl. Sci. Technol. 50 (2013) 314–320. https://doi.org/10.1080/00223131.2013.772446.
18. B. Leng, S. Ukai, Y. Sugino, Q. Tang, T. Narita, S. Hayashi, F. Wan, S. Ohtsuka, T. Kaito, Recrystallization Texture of Cold-rolled Oxide Dispersion Strengthened Ferritic Steel, ISIJ Int. 51 (2011) 951–957. https://doi.org/10.2355/isijinternational.51.951.
19. L. Autones, P. Aubry, J. Ribis, H. Leguy, A. Legris, Y. de Carlan, Assessment of Ferritic ODS Steels Obtained by Laser Additive Manufacturing, Materials. 16 (2023) 2397. https://doi.org/10.3390/ma16062397.
20. G. Spartacus, J. Malaplate, F. De Geuser, D. Sornin, A. Gangloff, R. Guillou, A. Deschamps, Nano-oxide precipitation kinetics during the consolidation process of a ferritic oxide dispersion strengthened steel., Scr. Mater. 188 (2020) 10–15. https://doi.org/10.1016/j.scriptamat.2020.07.003.
21. A. Deschamps, F. De Geuser, On the validity of simple precipitate size measurements by small-angle scattering in metallic systems, J. Appl. Crystallogr. 44 (2011) 343–352. https://doi.org/10.1107/S0021889811003049.
22. V. Gerold, G. Kostorz, Small-angle scattering applications to materials science, J. Appl. Crystallogr. 11 (1978) 376–404. https://doi.org/10.1107/S0021889878013497.
23. A. Deschamps, F. De Geuser, J. Malaplate, D. Sornin, When do oxide precipitates form during consolidation of oxide dispersion strengthened steels?, J. Nucl. Mater. 482 (2016) 83–87. https://doi.org/10.1016/j.jnucmat.2016.10.017.
24. M. Dumont, L. Commin, I. Morfin, F. DeGeuser, F. Legendre, P. Maugis, Chemical composition of nano-phases studied by anomalous small-angle X-ray scattering: Application to oxide nano-particles in ODS steels, Mater. Charact. 87 (2014) 138–142. https://doi.org/10.1016/j.matchar.2013.11.008.
25. T. Ungár, A. Borbély, The effect of dislocation contrast on x-ray line broadening: A new approach to line profile analysis, Appl. Phys. Lett. 69 (1996) 3173–3175. https://doi.org/10.1063/1.117951.
26. A. Borbély, J. Dragomir-Cernatescu, G. Ribárik, T. Ungár, Computer program *ANIZC* for the calculation of diffraction contrast factors of dislocations in elastically anisotropic cubic, hexagonal and trigonal crystals, J. Appl. Crystallogr. 36 (2003) 160–162. https://doi.org/10.1107/S0021889802021581.
27. H. Zhang, B. Johansson, L. Vitos, Ab initio calculations of elastic properties of bcc Fe-Mg and Fe-Cr random alloys, Phys. Rev. B. 79 (2009) 224201. https://doi.org/10.1103/PhysRevB.79.224201.
28. A. Borbély, The modified Williamson-Hall plot and dislocation density evaluation from diffraction peaks, Scr. Mater. 217 (2022) 114768. https://doi.org/10.1016/j.scriptamat.2022.114768.
29. A. Borbély, A. Aoufi, D. Becht, X-ray methods for strain energy evaluation of dislocated crystals, J. Appl. Crystallogr. 56 (2023) 254–262. https://doi.org/10.1107/S1600576722012262.
30. D. Hull, D.J. Bacon, Introduction to dislocations, 5. ed, Butterworth Heinemann, Elsevier, Amsterdam Heidelberg, 2011.
31. T. Okuda, M. Fujiwara, Dispersion behaviour of oxide particles in mechanically alloyed ODS steel, J. Mater. Sci. Lett. 14 (1995) 1600–1603. https://doi.org/10.1007/BF00455428.

32. J. Ribis, Y. de Carlan, Interfacial strained structure and orientation relationships of the nanosized oxide particles deduced from elasticity-driven morphology in oxide dispersion strengthened materials, Acta Mater. 60 (2012) 238–252. https://doi.org/10.1016/j.actamat.2011.09.042.
33. J. Ribis, M.A. Thual, T. Guilbert, Y. de Carlan, A. Legris, Relaxation path of metastable nanoclusters in oxide dispersion strengthened materials, J. Nucl. Mater. 484 (2017) 183–192. https://doi.org/10.1016/j.jnucmat.2016.12.007.
34. J. Ribis, M.-L. Lescoat, S.Y. Zhong, M.-H. Mathon, Y. de Carlan, Influence of the low interfacial density energy on the coarsening resistivity of the nano-oxide particles in Ti-added ODS material, J. Nucl. Mater. 442 (2013) S101–S105. https://doi.org/10.1016/j.jnucmat.2012.10.051.
35. G. Spartacus, J. Malaplate, F. De Geuser, I. Mouton, D. Sornin, M. Perez, R. Guillou, B. Arnal, E. Rouesne, A. Deschamps, Chemical and structural evolution of nano-oxides from mechanical alloying to consolidated ferritic oxide dispersion strengthened steel, Acta Mater. 233 (2022) 117992. https://doi.org/10.1016/j.actamat.2022.117992.
36. M. Ratti, D. Leuvrey, M.H. Mathon, Y. De Carlan, Influence of titanium on nano-cluster (Y, Ti, O) stability in ODS ferritic materials, J. Nucl. Mater. 386–388 (2009) 540–543. https://doi.org/10.1016/j.jnucmat.2008.12.171.
37. S.Y. Zhong, J. Ribis, V. Klosek, Y. De Carlan, N. Lochet, V. Ji, M.H. Mathon, Study of the thermal stability of nanoparticle distributions in an oxide dispersion strengthened (ODS) ferritic alloys, J. Nucl. Mater. 428 (2012) 154–159. https://doi.org/10.1016/j.jnucmat.2011.12.028.
38. F.J. Humphreys, M. Hatherly, Recrystallization and Related Annealing Phenomena., Elsevier Science, 2012.
39. B. Hary, M. van Der Meer, R. Logé, T. Baudin, Y. De Carlan, Optimization of the thermomechanical treatment to achieve a homogeneous microstructure in a 14cr ODS steel, (2017). https://hal.science/hal-02419649.
40. M. Serrano, A. García-Junceda, R. Hernández, M.H. Mayoral, On anisotropy of ferritic ODS alloys, Mater. Sci. Technol. 30 (2014) 1664–1668. https://doi.org/10.1179/1743284714Y.0000000552.
41. S. Ukai, S. Mizuta, T. Yoshitake, T. Okuda, M. Fujiwara, S. Hagi, T. Kobayashi, Tube manufacturing and characterization of oxide dispersion strengthened ferritic steels, J. Nucl. Mater. 283–287 (2000) 702–706. https://doi.org/10.1016/S0022-3115(00)00114-8.
42. D. Raabe, K. Lücke, Rolling and Annealing Textures of BCC Metals, Mater. Sci. Forum. 157–162 (1994) 597–610. https://doi.org/10.4028/www.scientific.net/MSF.157-162.597.
43. L.A.I. Kestens, H. Pirgazi, Texture formation in metal alloys with cubic crystal structures, Mater. Sci. Technol. 32 (2016) 1303–1315. https://doi.org/10.1080/02670836.2016.1231746.
44. W. Pantleon, Resolving the geometrically necessary dislocation content by conventional electron backscattering diffraction, Scr. Mater. 58 (2008) 994–997. https://doi.org/10.1016/j.scriptamat.2008.01.050.
45. M.F. Ashby, The deformation of plastically non-homogeneous materials, Philos. Mag. 21 (1970) 399–424. https://doi.org/10.1080/14786437008238426.
46. D.P. Field, P.B. Trivedi, S.I. Wright, M. Kumar, Analysis of local orientation gradients in deformed single crystals, Ultramicroscopy. 103 (2005) 33–39. https://doi.org/10.1016/j.ultramic.2004.11.016.
47. U.F. Kocks, A. AS, A. MF, Thermodynamics and kinetics of slip, (1975).
48. G. Fribourg, Y. Bréchet, A. Deschamps, A. Simar, Microstructure-based modelling of isotropic and kinematic strain hardening in a precipitation-hardened aluminium alloy, Acta Mater. 59 (2011) 3621–3635. https://doi.org/10.1016/j.actamat.2011.02.035.
49. D. Tabor, The hardness of metals, Clarendon Press; Oxford University Press, Oxford : New York, 2000.
50. J.R. Cahoon, W.H. Broughton, A.R. Kutzak, The determination of yield strength from hardness measurements, Metall. Trans. 2 (1971) 1979–1983. https://doi.org/10.1007/BF02913433.
51. C.E. Lacy, M. Gensamer, The tensile properties of alloyed ferrites, Trans AsM. 32 (1944) 88–110.
52. J.W. Martin, Micromechanisms in particle-hardened alloys, Cambridge university press, 1980.
53. S. Dangwal, K. Edalati, R.Z. Valiev, T.G. Langdon, Breaks in the Hall–Petch Relationship after Severe Plastic Deformation of Magnesium, Aluminum, Copper, and Iron, Crystals. 13 (2023) 413. https://doi.org/10.3390/cryst13030413.
54. B. Srinivasarao, K. Oh-Ishi, T. Ohkubo, K. Hono, Bimodally grained high-strength Fe fabricated by mechanical alloying and spark plasma sintering, Acta Mater. 57 (2009) 3277–3286.
55. L.P. Kubin, A. Mortensen, Geometrically necessary dislocations and strain-gradient plasticity: a few critical issues, Scr. Mater. 48 (2003) 119–125. https://doi.org/10.1016/S1359-6462(02)00335-4.
56. Y. Ateba Betanda, A.-L. Helbert, F. Brisset, M.-H. Mathon, T. Waeckerlé, T. Baudin, Measurement of stored energy in Fe–48%Ni alloys strongly cold-rolled using three approaches: Neutron diffraction, Dillamore and KAM approaches, Mater. Sci. Eng. A. 614 (2014) 193–198. https://doi.org/10.1016/j.msea.2014.07.037.
57. S. Birosca, G. Liu, R. Ding, J. Jiang, T. Simm, C. Deen, M. Whittaker, The dislocation behaviour and GND development in a nickel based superalloy during creep, Int. J. Plast. 118 (2019) 252–268. https://doi.org/10.1016/j.ijplas.2019.02.015.
58. C. Zhu, T. Harrington, G.T. Gray, K.S. Vecchio, Dislocation-type evolution in quasi-statically compressed polycrystalline nickel, Acta Mater. 155 (2018) 104–116. https://doi.org/10.1016/j.actamat.2018.05.022.
59. M. Wilkens, Fundamental Aspects of Dislocation Theory, Natl Bur. Stand. U.S. Spec. Publ. Vol. 317, 1970.

60. N. Ridley, H. Stuart, Lattice parameter anomalies at the Curie point of pure iron, J. Phys. Appl. Phys. 1 (1968) 1291–1295. https://doi.org/10.1088/0022-3727/1/10/308.
61. E.V. Kozlov, N.A. Koneva, Internal fields and other contributions to flow stress, Mater. Sci. Eng. A. 234–236 (1997) 982–985. https://doi.org/10.1016/S0921-5093(97)00381-X.
62. H. Mughrabi, The α-factor in the Taylor flow-stress law in monotonic, cyclic and quasi-stationary deformations: Dependence on slip mode, dislocation arrangement and density, Curr. Opin. Solid State Mater. Sci. 20 (2016) 411–420. https://doi.org/10.1016/j.cossms.2016.07.001.